Composition Dependence of the Band Gap and Doping in Cu₂O-Based Alloys as Predicted by an Extension of the Dilute-Defect Model

Vladan Stevanović,[1,2] Andriy Zakutayev,[2] and Stephan Lany[2,*]

[1]*Colorado School of Mines, Golden, Colorado 80401, USA*
[2]*National Renewable Energy Laboratory, Golden, Colorado 80401, USA*

Tuning the optoelectronic properties through alloying is essential for semiconductor technology. Currently, mostly isovalent and isostructural alloys are used (e.g., groups IV and III-V), but a vast and unexplored space of novel functional materials is conceivable when considering more complex alloys by mixing aliovalent and heterostructural constituents. The real challenge lies in the quantitative property prediction for such complex alloys to guide their experimental exploration. We develop an approach to predict compositional dependence of both band-structure and electrical properties from *ab initio* calculations by extending the conventional dilute-defect model to higher (alloy) concentrations. Considering alloying of aliovalent (Mg, Zn, Cd) cations and isovalent anions (S, Se) into Cu₂O, we predict tunability of band-gap energies and doping levels over a wide range, including the type conversion from *p* to *n* type. Initial synthesis and characterization of Zn-and Se-substituted Cu₂O support the defect model, suggesting these alloys as promising novel oxide-semiconductor materials.

I. INTRODUCTION

Semiconductor alloys are typically mixtures of two isovalent and isostructural materials, e.g., $Si_{1-x}Ge_x$ in microelectronics [1,2], $Ga_{1-x}In_xN$ for blue light-emitting diodes [3], or $Cd_{1-x}Zn_xTe$ for radiation detectors [4]. In photovoltaics, the solar cells with the highest conversion efficiencies above 40% are multijunction devices with many layers of carefully engineered III-V alloys grown on a Ge substrate [5]. Whereas isovalent alloying typically employs compositions from a few percent up to equal amounts of the constituents, so to modify the band-structure and optical properties, nonisovalent impurity doping [6] is used to tailor the electrical properties via more dilute substitutions ranging from parts per million (approximately 10^{16} cm^{-3}) up to a few percent in transparent conducting oxides [7].

Accordingly, standard theoretical approaches of electronic structure calculations usually address either the modification of band-structure properties due to alloying [8–10] or the manipulation of electrical properties due to doping [11–13]. However, a more general approach to semiconductor alloys includes the possibility of mixing aliovalent and heterostructural materials. In this case, the variation of band-structure and electrical properties is inherently coupled, and methods for describing alloy formation enthalpies need to include the Fermi energy as an additional variable that affects the formation enthalpy of nonisovalent substituents and eventually determines the carrier (electron or hole)

concentrations in the alloy. A notable previous work in this regard is the study of Sm-doped CeO_2 by van de Walle and Ellis [14], where the valence mismatch between Ce^{+IV} and Sm^{+III} is accommodated by formation of charged oxygen-vacancy defects (V_O^{2+}) but without the generation of free carriers.

We approach the aliovalent alloy problem by extending the conventional dilute-impurity model to higher (alloy) concentrations and study aliovalent alloying of divalent cations (II = Mg, Zn, Cd) and isovalent chalcogenide anions (VI = S, Se) into a Cu₂O matrix. Specifically, we first calculate the formation energies of substitutional dopants and intrinsic defects in the dilute limit. Second, we determine the structures and binding energies of dopant-defect pairs and complexes. Third, knowing the energetically favorable defect structure, we determine the compositional dependence of the band-gap and band-edge energies, which affect the defect formation energies. Finally, based on these input data, we perform thermodynamic simulations for the net-doping concentrations as a function of the alloy composition. The results of these simulations are shown in Fig. 1, and we will describe the individual steps in detail below.

The Cu₂O parent compound has received considerable interest as one of the few prototypical *p*-type oxides [15–19], and the understanding of the band-structure and defect physics in Cu₂O is central to succeed in the quest for the so far elusive *p*-type transparent conductive oxides [20,21]. The *p*-type nature of Cu₂O has further spurred interest in the areas of magnetic semiconductors [22,23] and in regard to possible applications in photovoltaics [24,25] and photo-electrocatalysis [26]. However, as in case of the traditional
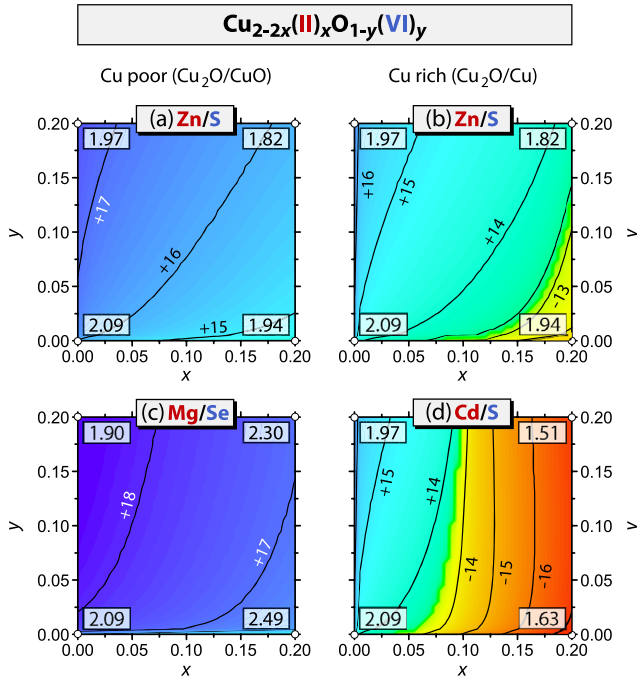
*Stephan.Lany@nrel.gov

FIG. 1. Thermodynamic modeling ($T = 400\,°C$) of the net doping $\log(|N_D - N_A|/\mathrm{cm}^{-3})$ in $\mathrm{Cu}_{2-2x}(\mathrm{II})_x\mathrm{O}_{1-y}(\mathrm{VI})_y$ alloys as a function of x and y for different II-VI combinations and growth conditions (Cu rich and poor). N_D and N_A are individual concentrations of donors and acceptors, respectively. The sign indicates the type of doping (positive for p type, negative for n type). The numbers in the corners stand for the predicted band gaps extrapolated according to Eq. (2) and are given for the end compositions for $0 \leq (x, y) \leq 0.2$.

semiconductor alloys, the controlled tailoring of the band-structure and electrical properties will be instrumental in realizing novel $\mathrm{Cu_2O}$-based technologies. In particular, ambipolar dopability will open a range of potential applications from oxide electronics to solar-energy generation.

II. APPROACH AND RESULTS

In order to theoretically predict both band-structure properties and electrical doping as a function of the alloy composition, we start from the conventional defect theory and supercell formalism [27–30] and then formulate an approach to extend the dilute-impurity model to the higher concentrations present in alloys. Within the standard dilute-defect model, the formation energy of a defect D in a charge state q is defined as

$$\Delta H_{D,q}(\Delta E_F, \{\Delta\mu_\alpha\}) = [E_{D,q} - E_H] + q(E_{\mathrm{VBM}} + \Delta E_F)$$
$$+ \sum_\alpha n_\alpha(\mu_\alpha^0 + \Delta\mu_\alpha) \quad (1)$$

and is a function of two types of variables: (i) ΔE_F measuring the Fermi energy E_F relative to the valence band maximum (VBM) of the host system and (ii) a set of chemical potentials $\{\Delta\mu_\alpha\}$ describing chemical reservoirs.

$E_{D,q}$ and E_H in Eq. (1) are the total energies of a system with and without the defect, respectively. The $\{\Delta\mu_\alpha\}$'s are defined relative to chemical potentials $\{\mu_\alpha^0\}$ of the pure elements in their reference phases and reflect the thermo-dynamic boundary conditions ranging between Cu poor and O rich ($\mathrm{CuO/Cu_2O}$ coexistence) to Cu rich and O poor ($\mathrm{Cu/Cu_2O}$). For an accurate prediction of the defect formation energies, we use a recently introduced and tested approach [31] that combines supercell calculation using density functional theory (DFT) with band-gap corrections from GW quasiparticle energy calculations. Further details of our computational approach are given in Appendix A.

With an increasing concentration of dopants beyond the dilute limit, two effects become more prominent: First, the interaction between dopants and defects can lead to the formation of pairs and larger complexes. Thus, we calculate the different configurations of dopant-defect pairs and their binding energies and take into account their association and dissociation within the thermodynamic modeling, using the law of mass action [32]. Second, since the band structure changes with the chemical composition, we need to take into account the composition dependence of the individual band-edge energies (E_{VBM} and E_{CBM}, where CBM denotes conduction-band maximum), which control the formation energies of ionized (charged) defects and dopants [cf. Eq. (1)].

III. ENERGETICS OF POINT DEFECTS AND DEFECT PAIRS

In order to develop a complete defect model for the underlying cuprite structure of $\mathrm{Cu_2O}$, we consider the intrinsic defects, i.e., the cation and anion vacancies and interstitials, the extrinsic cation and anion substitutions, as well as defect pairs and complexes between the low-energy species, up to three constituents. Figure 2(c) shows the defect-formation energies of the most relevant point defects and defect pairs, as a function of the Fermi energy at the Cu-poor–O-rich conditions and for the particular II = Zn and VI = S choice. The chemical potential of Zn is limited by the formation of ZnO. The other considered cases of II = Mg, Cd and VI = Se present a qualitatively similar picture. The full list of calculated formation energies is given in Appendix A. The shaded areas in Fig. 2(c) denote the band-edge shifts ΔE_{VBM} and ΔE_{CBM} determined from GW calculations [33]. Since oxygen vacancies stay in the electrically inactive neutral charge state irrespective of the Fermi level [15] and do not show strong binding to other defects, we will not further discuss them.

$\mathrm{Zn_{Cu}}$ is an electrically active donor-type defect (divalent Zn substituting for monovalent Cu) that assumes a positively charged state for most Fermi energies, and which has a shallow donor level about 0.18 eV below the conduction-band minimum. This ionization energy is consistent with the expectations from effective mass theory for $m_e^*/m_0 = 1.0$
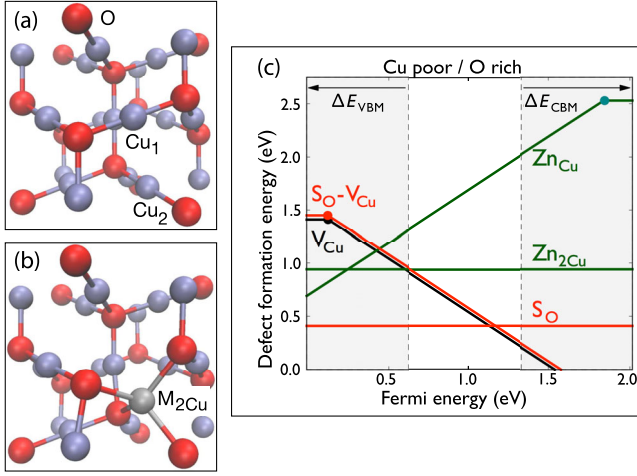
FIG. 2. (a) Cuprite Cu_2O structure with O atoms shown in red and Cu in blue; (b) structure of a $(II)_{2Cu}$ defect pair, where one metal impurity (II = Mg, Zn, Cd) shown in gray replaces two copper atoms Cu_1 and Cu_2; (c) defect and defect-pair formation energies for V_{Cu}, group-II cation impurities (II = Zn) and group-VI anion impurities (VI = S) as a function of the Fermi energy, assuming phase coexistence of Cu_2O with ZnO and Cu_2S.

and $\varepsilon = 7.5$ [34]. The positively charged Zn_{Cu}^{+} attracts negatively charged V_{Cu}^{-} resulting in the formation of the electrically neutral Zn_{2Cu} defect complex in which Zn substitutes two Cu atoms and occupies an interstitial site that is fourfold coordinated by oxygen as shown in Fig. 2(b). This configuration is akin to the Cu vacancy in the "split-vacancy" configuration (one interstitial Cu replaces two lattice Cu atoms), which is a metastable configuration about 0.3 eV higher in energy than the vacancy at the Cu lattice site in agreement with Refs. [15,35]. Here, however, the Zn_{2Cu} configuration is the ground state (in agreement with the findings reported in Ref. [36]), which accommodates the preferential tetrahedral coordination of Zn inside the cuprite lattice and lies about 0.80 eV lower in energy than the $(Zn_{Cu}\text{-}V_{Cu})$ pair. Analogous defect complexes are formed by the other group-II elements Mg and Cd. Further, the isovalent S_O and Se_O defects bind Cu vacancies, which can be understood as resulting from compensation of the tensile (S_O and Se_O) and compressive strain (V_{Cu}) induced by the defects. The binding energies relative to the isolated dopants and defects are given in Table I.

TABLE I. Calculated binding energies of defect pairs formed between the isolated (II) and (VI) dopants and Cu vacancies.

Defect reaction	Binding energy (eV)
$Mg_{Cu}^{+} + V_{Cu}^{-} \rightarrow Mg_{2Cu}$	−2.13
$Zn_{Cu}^{+} + V_{Cu}^{-} \rightarrow Zn_{2Cu}$	−1.29
$Cd_{Cu}^{+} + V_{Cu}^{-} \rightarrow Cd_{2Cu}$	−1.24
$S_O + V_{Cu}^{-} \rightarrow (S_O\text{-}V_{Cu})^{-}$	−0.37
$Se_O + V_{Cu}^{-} \rightarrow (Se_O\text{-}V_{Cu})^{-}$	−0.72

TABLE II. The parameters α (eV) describing the composition dependence of the band-edge and -gap energies, according to Eq. (2).

	α_{VBM}	α_{CBM}	α_g
II = Mg	−1.88	+0.12	+2.00
II = Zn	−0.59	−1.32	−0.73
II = Cd	−0.97	−3.26	−2.30
VI = S	+0.33	−0.30	−0.62
VI = Se	+0.06	−0.88	−0.95

IV. COMPOSITION OF DEPENDENCE OF THE BAND-EDGE ENERGIES

In addition to defect pairing, a second effect that needs to be taken into account when extending the dilute-defect model to larger concentrations is the composition dependence of the band-edge energies. Similar to the case of the GW quasiparticle energy shifts [see Fig. 2(c)], the charged-defect formation energies vary with a change of the VBM and CBM energies with composition. The band-gap and band-edge shifts in a $Cu_{2-2x}(II)_xO_{1-y}(VI)_y$ alloy can then be expressed by a linear expansion

$$E_g(x, y) = E_g^0 + \alpha_g^{II}x + \alpha_g^{VI}y \qquad (2)$$

and similar expressions with α_{VBM} and α_{CBM} for the individual band edges. The α parameters determined from GW calculations in supercells containing $(II)_{2Cu}$ and $(IV)_O$ substitutions are given in Table II. We note that none of the (II) and (VI) dopants introduce resonant states close to the band-edge energies, which could cause large bowing effects, like, e.g., in N-doped GaAs [37]. Thus, the linear expansion Eq. (2) can be expected to be a good approximation within the low-to-moderate composition range up to $x, y \leq 0.2$ considered here. Having the α parameters allows us to predict directly the defect formation energies of $Cu_{2-2x}(II)_xO_{1-y}(VI)_y$ alloys using the defect formation energies from the pure Cu_2O computed from Eq. (1) and the composition-dependent band edges from Eq. (2). We test the applicability and accuracy of this model by performing direct defect calculations on actual alloy compositions as shown in Appendix C.

V. THERMODYNAMIC MODELING OF DEFECT CONCENTRATIONS AND DOPING

Using the calculated formation energies of point defects and defect pairs, as well as their composition dependence, we perform thermodynamic simulations to determine the concentrations of the substituted elements and the V_{Cu} defects. Under equilibrium conditions, the site concentration of a defect D, i.e., the concentration of defects divided by that of the lattice sites on which the defect resides, is given approximately by $[D] = \exp(-\Delta H_D/k_BT)$. Because of the Fermi-level dependence of ΔH_D in the case of

electrically active defects or dopants [cf. Eq. (1)], ΔE_F needs to be solved together with the defect concentrations, which is achieved by a numerical self-consistent solution under the constraint of overall charge neutrality between charged defects and carriers (free electrons and holes) [28,38]. In the present work, we further take into account the association and dissociation of defect pairs within the self-consistent solution, as described in Ref. [32]. The thermodynamics of the association and dissociation of defect pairs is described by the law of mass action, e.g.,

$$[\mathrm{Zn_{2Cu}}] = [\mathrm{Zn_{Cu}}][V_{Cu}] \exp[-E_b(\mathrm{Zn_{2Cu}})/k_B T],$$
$$[(\mathrm{S_O} - V_{Cu})] = [\mathrm{S_O}][V_{Cu}] \exp[-E_b(\mathrm{S_O} - V_{Cu})/k_B T], \quad (3)$$

where the brackets denote the site concentrations of the respective species and include the multiplicity of the equivalent configurations of the defect pairs [32]. The electrical properties are characterized by the common "net-doping concentration," i.e., the difference $N_D - N_A$ between the total donor and acceptor concentrations. In the following, we apply this model to three situations: (i) the intrinsic doping of pure Cu_2O due to V_{Cu} formation, (ii) the equilibrium solubility limits of the group-II and -VI dopants, and (iii) the composition dependence of electrical properties in alloys at nonequilibrium compositions.

As shown in Fig. 3, we find that in pure Cu_2O, the V_{Cu} concentration varies between the mid-10^{15}-to mid-10^{16}-cm^{-3} range between the Cu-rich (Cu_2O/Cu) and Cu-poor (Cu_2O/CuO) conditions at $T = 450\,°C$, agreeing well with the hole-carrier density of about 10^{15} cm^{-3} measured in Cu_2O sheets quenched from this temperature [24,39]. In order to determine the solubility limits of the

group-II and -VI dopants, we take into account the constraints to their chemical potentials arising from phase separation and the ensuing precipitation of the competing phases, i.e., MgO, ZnO, CdO, Cu_2S, and Cu_2Se. As seen in Fig. 3, the resulting equilibrium solubilities can exceed 10^{20} cm^{-3} but remain in the range of dilute doping below the percent range. Since the dominant defect configurations, i.e., the $(\mathrm{VI})_O$ substitution and the $(\mathrm{II})_{2Cu}$ pair, are charge neutral [cf. Fig. 2(c)], and since the effect on the band energies is minute at such low concentrations, the electrical properties do not significantly change compared to pure Cu_2O.

The solubility limits of dopants can often be overcome by nonequilibrium techniques, such as low-temperature thin-film growth [40,41]. In fact, the dopant concentrations are often supersaturated, and the solubility limits are attained only after prolonged annealing procedures at high temperatures [42]. Similarly, in alloys where the positive mixing enthalpy creates a "miscibility gap" in equilibrium, such compositions can nevertheless be realized under synthesis conditions where the long-range diffusion necessary for phase separation is kinetically limited [43] with low-temperature nonequilibrium growth as a potential path to realize such aliovalent alloys [44]. In the case of heterostructural alloys, the lattice mismatch provides a further barrier for nucleation of secondary phases. Thus, we are now addressing the question of which range of band gaps and electrical doping can be achieved in $Cu_{2-2x}(\mathrm{II})_x O_{1-y}(\mathrm{VI})_y$ if the alloy composition is treated as a parameter that can exceed the thermodynamic solubility limit. To this end, we perform the thermodynamic modeling for a partial equilibrium [45], in which the constraints due to phase separation and precipitation are omitted. In practice, the dopant chemical potential is adjusted during the thermodynamic simulation until the respective alloy composition is attained. This situation corresponds to a supersaturation of dopants; i.e., the dopant chemical potential is higher and the respective defect formation energy is lower than in the unconstrained equilibrium where the precipitation of secondary phases (e.g., ZnO, Cu_2S, etc.) limits the solubility. The balance between electrically active dopants and the compensating intrinsic defects determines the electrical properties. Such partial equilibrium simulations have recently explained successfully the temperature dependence of the conductivity in Ga-doped ZnO [46].

The contour plot in Fig. 1 shows the net-doping $\log(|N_D - N_A|/\mathrm{cm}^{-1})$ in $Cu_{2-2x}(\mathrm{II})_x O_{1-y}(\mathrm{VI})_y$ alloys as a function of x and y (N_D and N_A stand for the concentration of donors and acceptors, respectively). The numbers in the corners give the predicted band gaps for the respective end-point compositions according to Eq. (2) and the data in Table II. For the Zn-S combination, we show the net doping for both Cu-poor (equilibrium between Cu_2O and CuO) and Cu-rich (equilibrium between Cu_2O
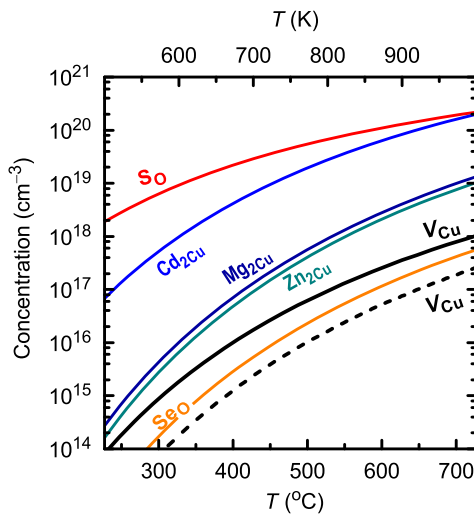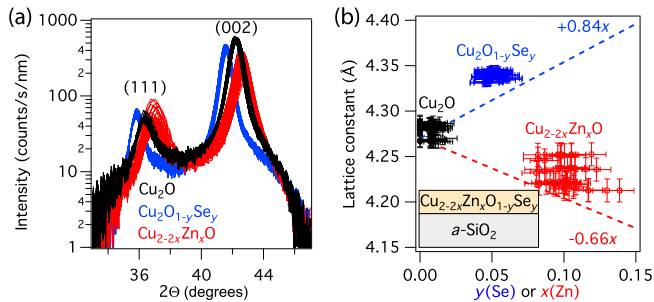

FIG. 3. Thermodynamic modeling of defect and dopant concentrations in Cu_2O. Solid lines show the solubility limits under Cu-poor (Cu_2O/CuO boundary) conditions. The dashed line shows the V_{Cu} concentration under Cu-rich conditions (Cu_2O/Cu boundary).

FIG. 4. (a) X-ray-diffraction patterns of Cu_2O (black), $Cu_{2-2x}Zn_xO$ (red), and $Cu_2O_{1-y}Se_y$ (blue) thin films on a-SiO_2, 44 patterns each. (b) Lattice constant of Cu_2O (black), $Cu_{2-2x}Zn_xO$ (red), and $Cu_2O_{1-y}Se_y$ (blue) alloys from experiment (symbols) and computations (lines).

and Cu) conditions, thereby illustrating the dependence on the growth conditions. The combinations Mg-Se and Cd-S are shown for the Cu-poor and Cu-rich conditions, respectively, thereby emphasizing the most pronounced p-type (due to Se) and n-type (due to Cd) doping scenarios. Within the composition range $0 \leq x, y \leq 0.2$, we obtain band gaps between 1.44 eV (for the Cd/Se combination at $x = y = 0.2$, not shown in Fig. 1) and 2.49 eV (for Mg alloying at $x = 0.2$). The complete data set including all II-VI combinations is given in Appendix B.

VI. EXPERIMENTAL SYNTHESIS

As a first step towards the experimental realization of these novel functional Cu_2O alloys, we use a combinatorial synthesis and characterization approach [47] to grow thin films of Cu_2O, $Cu_{2-2x}Zn_xO$, and $Cu_2O_{1-y}Se_y$ [48] and to characterize these films in a spatially resolved way [41] using x-ray diffraction. Figure 4(a) shows the x-ray-diffraction data for pure Cu_2O, for varying Zn substitution centered around $x = 0.10$ and for varying Se substitution centered around $y = 0.06$. No impurity phases of ZnO or Cu_2Se are observed. The measured composition dependence of the lattice constant is compared with the prediction of the defect model in Fig. 4(b). The trend of a reduction of the lattice constant due to Zn alloying and an increase due to Se alloying is observed in both the experimental and theoretical data sets, suggesting that the alloyed elements are incorporated in the cuprite lattice as described by the computational defect model, instead of forming secondary phases. Note that the presence of residual strain in the films leads to a slightly larger lattice constant of Cu_2O than in single crystals, where $a = 4.27$ Å, and that the present type of DFT calculations cause a typical but not exactly systematic overestimation of the lattice constant by about 1%.

VII. DISCUSSION

The extension of the traditional dilute-defect model towards larger alloy concentrations enables the prediction

of doping in aliovalent alloys, thereby opening a path to design the electrical properties in complex semiconductor materials. Notably, the electrical behavior of the $Cu_{2-2x}(II)_xO_{1-y}(VI)_y$ alloys differs markedly from the traditional doping mechanism [6], where aliovalent impurity atoms introduce a number of charge carriers that is comparable to the number of dopant atoms (although a certain reduction from unity doping efficiency is often caused by self-compensation [49]).

Our model predicts an interesting and counterintuitive doping behavior, in that the aliovalent group-II dopants have a negligible effect on the electrical properties at typical subpercent doping levels (see Fig. 1) but modify the band gap at higher alloylike concentrations. On the other hand, the isovalent group-VI substitution has a rather modest effect on the band gap but increases the hole-carrier concentration significantly. This rather ironic behavior is explained by the important role of dopant-defect interactions in this system: The divalent dopants incorporate dominantly in the form of a valence-conserving defect complex, e.g., Zn_{2Cu}, where one Zn^{+II} replaces two Cu^{+I} ions. This charge-neutral complex is electrically inactive, but it modifies the band structure. As seen in Table II, Mg alloying lowers the VBM energy, which can be explained by the fact that Mg lacks an occupied d shell and, therefore, reduces the density of states at the Cu-d-like top of the valence band. Zn and Cd introduce delocalized, unoccupied s-like states, which cause a lowering of the CBM energy. The isovalent dopants have a smaller effect on the band structure but affect the electrical properties. The binding energy between substitutional S_O or Se_O dopants and Cu vacancy V_{Cu} effectively reduces the formation enthalpy of these hole-producing defects when forming close to the isovalent dopant, thereby increasing the p-type doping with increasing S-SE alloying.

We considered the range $0 \leq x, y \leq 0.2$ as a composition range within which the realization of $Cu_{2-2x}(II)_xO_{1-y}(VI)_y$ alloys can be achievable by nonequilibrium growth methods. Within this composition window, we obtain predicted band-gap energies between 1.4 ($x_{Cd} = y_{Se} = 0.2$) and 2.5 eV ($x_{Mg} = 0.2$) from the values given in Table II, compared to the 2.1-eV room-temperature gap of Cu_2O [50]. Whereas the binary-oxide Cu_2O is always p type conducting within a narrow window $p = 10^{14}-10^{16}$ cm^{-3} [25,39,51], we find the alloying approach allows a much better control of the electrical properties. Because of the pronounced dopant-defect interaction, alloying of S and Se increases the p-type doping, up to the 10^{18} cm^{-3} range for $y_{Se} > 0.02$ (Fig. 1). For the case of cation doping, the formation of dopant-defect complexes like Zn_{2Cu} prevents effective n-type doping. However, at very high concentrations of Zn or Cd beyond the dilute doping regime, i.e., in the aliovalent alloying regime, we observe type conversion from p to n type with a maximal electron doping level of $N_D - N_A = 2 \times 10^{17}$ cm^{-3} at $x_{Cd} = 0.2$ (see Fig. 1).

The physical origin of the type conversion from p to n type is a combination of two causes. First, the increased nonequilibrium chemical potential of the group-II element effectively lowers the formation energy of the $(II)_{Cu}$ donors, which, otherwise, is rather high [see Fig. 2(c)]. Note that most II elements are still incorporated as charge-neutral $(II)_{2Cu}$ defect pairs, and only a fraction forms as a substitutional donor, e.g., Cd_{Cu}, as determined by the law of mass action [see Eq. (3)]. In fact, only a fraction of about 10^{-6} of alloyed Cd atoms become electrically active as n-type dopants. The second effect is the lowering of the CBM energy with the x composition for Zn and Cd, which supports n-type doping by bringing the CBM closer to the equilibrium Fermi level during the thermodynamic simulation. This effect is most pronounced for Cd alloying which affords the largest reduction of the CBM energy, as seen in the α_{CBM} parameter in Table II, and which is the only group-II dopant that can be expected to produce robust n-type doping with appreciable carrier densities (Fig. 1).

The synthesis and characterization of Zn- and Se-substituted Cu_2O alloys shows no indication of impurity phases (ZnO or Cu_2Se), and the composition dependence of the lattice parameter is consistent with the computational defect model. Thus, the initial experimental data support the viability of the proposed alloy system.

VIII. CONCLUSIONS

In conclusion, the band-structure and electrical properties of complex $Cu_{2-2x}(II)_xO_{1-y}(VI)_y$ alloys are modeled by extending the dilute-defect model to finite alloy compositions, taking into account pair and complex formation between of dopants and defects, as well as the composition dependence of the band-edge energies. In contrast to conventional semiconductor systems, where the manipulation of band-structure properties via isovalent alloying is independent from the control of electrical properties via dilute aliovalent doping, the two mechanisms become intertwined due to the dopant-defect interactions. Considering the alloying of aliovalent (Mg, Zn, Cd) cations and isovalent anions (S, Se) into Cu_2O, we predict that the band-gap energies and the doping levels are tunable over a wide range (gap from 1.4 to 2.5 eV, carriers from $p = 10^{18}$ cm^{-1} to $n = 2 \times 10^{17}$ cm^{-1}), including the type conversion from p to n type. The initial thin-film synthesis and characterization of these novel oxide-semiconductor materials shows a single-phase formation beyond the thermodynamic solubility limit, thereby supporting the underlying defect model. The $Cu_{2-2x}(II)_xO_{1-y}(VI)_y$ alloys could find application, e.g., as alternative earth-abundant photovoltaic materials.

ACKNOWLEDGMENTS

APPENDIX A: METHODS

1. Theory and modeling

All DFT calculations are performed with the projector augmented-wave (PAW) method [52] as implemented in the VASP code [53], employing the Perdew-Burke-Ernzerhof (PBE) exchange-correlation functional [54], and the DFT $+ U$ formulation of Ref. [55], with $U = 5$ eV for Cu d orbitals. Defects and defect pairs are modeled in large supercells of Cu_2O with 162 atoms, applying the standard finite-size corrections for image charge interactions and potential alignment [45]. The band-gap problem is resolved by combining the DFT supercell energies with the results from GW quasiparticle energy calculations as described in Ref. [31], using the band-edge shifts $\Delta E_{VBM} = -0.62$ eV and $\Delta E_{CBM} = +0.68$ eV, as determined in a recent GW study of transition metal oxides [33]. In order to accurately describe the chemical potentials $\{\Delta\mu_\alpha\}$ entering in Eq. (1), we use the fitted elemental reference energies of Ref. [56]. For the host atoms Cu and O, the chemical potentials are limited by the phase coexistence of Cu_2O with CuO (Cu-poor–O-rich condition; $\Delta\mu_{Cu} = -0.24$ eV and $\Delta\mu_O = -1.38$ eV) and with metallic Cu (Cu-rich/O-poor condition; $\Delta\mu_{Cu} = 0.00$ eV and $\Delta\mu_O = -1.86$ eV). For the thermodynamic solubility limits, the chemical potentials $\{\Delta\mu_\alpha\}$ of the extrinsic impurities are determined by the condition of phase coexistence with the related secondary phases, e.g., MgO, ZnO, CdO, Cu_2S, and Cu_2Se. All defect formation energies for the charge-neutral defects and defect pairs given for $\Delta\mu_\alpha = 0$ are provided in Table III.

To determine the effect of $(II)_{2Cu}$ and $(VI)_O$ substitution on band-edge energies, we perform direct GW calculations in 48-atom supercells containing one of these defects. These GW calculations are performed analogously to those in Ref. [33] using the implementation of the GW method in the PAW framework Ref. [57].

We note that GW calculations are generally difficult to converge [58,59]. For the PAW implementation of the GW method, a recent work [60] has identified limitations due to basis-set incompleteness, which are particularly pronounced for d orbitals. We think it is likely that these issues lie behind the previously observed need to apply an external d-state potential in GW for transition metal compounds [33]. Including these potentials (here, $V_d = -2.4$, -1.5, and -0.5 eV for Cu, Zn, and Cd, respectively)

TABLE III. Calculated formation energies ΔH_D for the charge-neutral defects and defect pairs given for $\Delta \mu_\alpha = 0$, i.e., all chemical potentials set at the elemental reference phase. For the electrically active defects, the respective donor (D) or acceptor (A) ionization energies (ε_D or ε_A) are also given.

		ΔH_D [eV]	ε_D or ε_A [eV]
V_{Cu}	(A)	+1.65	0.13
Mg_{Cu}	(D)	−1.32	0.17
Zn_{Cu}	(D)	+0.59	0.18
Cd_{Cu}	(D)	+1.17	0.18
V_O		+2.42	(···)
S_O		+1.27	(···)
Se_O		+2.14	(···)
Mg_{2Cu}		−3.52	(···)
Zn_{2Cu}		−0.76	(···)
Cd_{2Cu}		−0.13	(···)
$(S_O\text{-}V_{Cu})$	(A)	+2.55	0.13
$(Se_O\text{-}V_{Cu})$	(A)	+3.07	0.13

mitigates these issues and should lead to fairly reliable valence-band shifts, as indicated by the good agreement of the calculated ionization potentials with the experimental data [61].

In order to calculate the doping and defect concentrations, we use a thermodynamic model [28,32,38], where a self-consistency condition is solved numerically for the formation energy $\Delta H_{D,q}$, the defect concentration, and the Fermi level ΔE_F under the constraint of overall charge neutrality. The case of the partial equilibrium is solved by adjusting the defect formation energy for atomic substitution or, equivalently, the dopant chemical potential, during the simulation until the respective alloy concentration is obtained. The temperature dependence of the Cu_2O band gap as determined in Ref. [62] is taken into account in the thermodynamic simulation. The calculated carrier densities in pure Cu_2O are in agreement with available experimental data [24,39] but about 2 orders of magnitude lower than those determined before in Ref. [15]. This difference results mostly from the GW quasiparticle energy shift of the VBM, which increases $\Delta H(V_{Cu}^-)$ by 0.62 eV relative to a standard DFT + U calculation.

2. Thin-film deposition

Thin films of Cu_2O, $Cu_{2-2x}Zn_xO$, and $Cu_2O_{1-y}Se_y$ are grown at ambient temperature by combinatorial RF cosputtering with a continuous composition spread [48] in an AJA International vacuum chamber with 10^{-10}-atm base pressure and filled with 10^{-6} atm of ultrahigh-purity Ar. We use (50×50)-mm Eagle-XG glass substrates and 50-mm diameter targets of Cu_2O, ZnO, and Cu_2Se. The films are characterized at 44 spatially distinct locations [41], determining the composition and thickness (350–650-nm range) by x-ray fluorescence and determining the phase composition and lattice constant by x-ray diffraction.

APPENDIX B: COMPLETE DATA OF THERMODYNAMIC MODELING

In Figs. 5–7 we provide the thermodynamic modeling results for all group-II and group-IV elements included in this work.
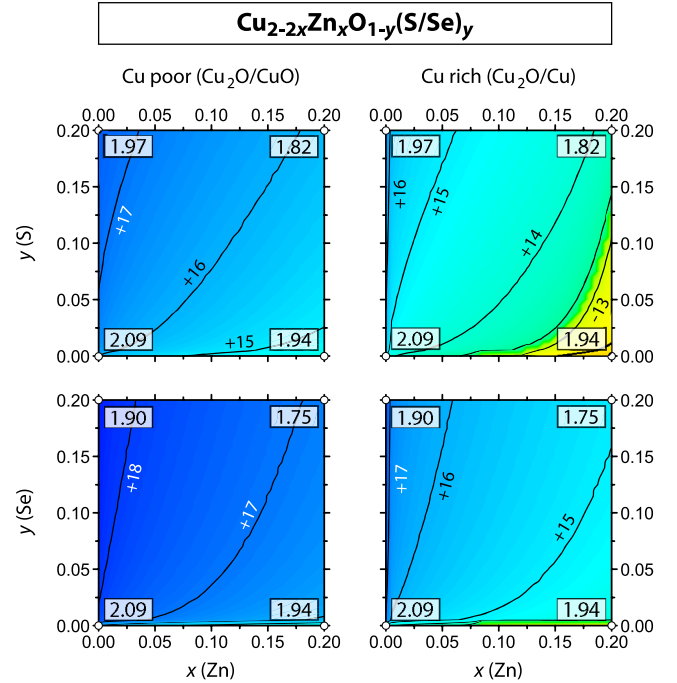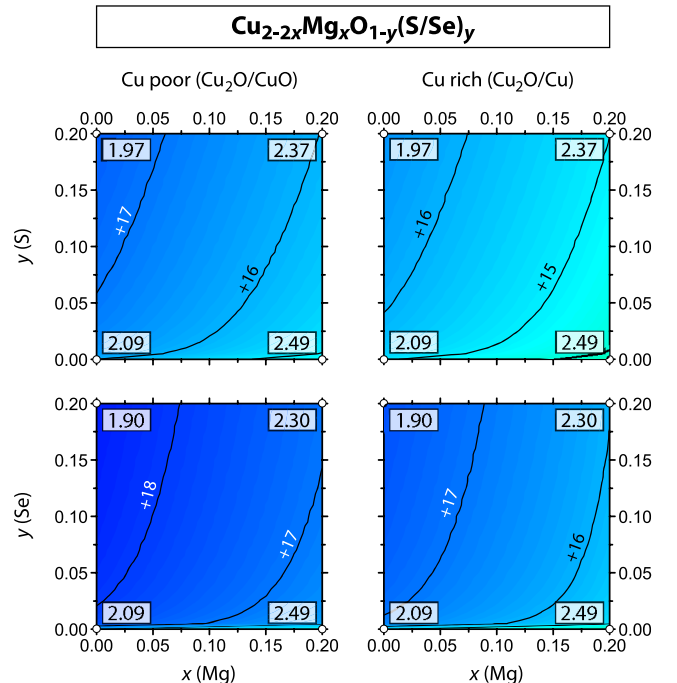
FIG. 5. Same as Fig. 1 but for (II) = Zn.

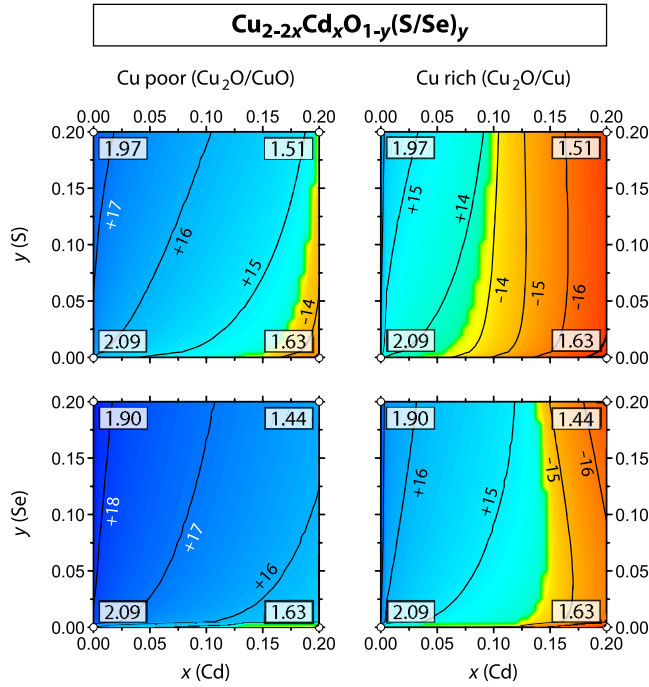FIG. 6. Same as Fig. 1 but for (II) = Mg.

FIG. 7.   Same as Fig. 1 but for (II) = Cd.

APPENDIX C: TEST OF ALLOY MODEL

The present work utilizes a model to determine to linear order the composition dependence of the band gap and the individual band-edge energies. Here we test this linear extrapolation by comparison with calculations of supercells that explicitly incorporate different alloy compositions. Specifically, we use 162-atom supercells containing four and eight cation or anion substitutions, e.g., Zn_{2Cu} or S_O with x or $y = 0.074$ and 0.148. In all cases, the results of two different random alloy representations are averaged. Since GW calculations for such large supercells are not feasible, we conduct the test of the model on the PBE + U

TABLE IV.   The parameters α (eV) describing the composition dependence of the band-edge energies, according to Eq. (2). Values are given for the DFT contribution $\alpha(PBE + U)$, and the additional contribution $\Delta\alpha(GW)$ from GW quasiparticle energy corrections. The sum of the respective contributions yields the values given in Table II.

	α_{VBM} (PBE + U)	α_{CBM} (PBE + U)	$\Delta\alpha_{VBM}$ (GW)	$\Delta\alpha_{CBM}$ (GW)
Mg_{2Cu}	−1.13	+0.40	−0.75	−0.28
Zn_{2Cu}	−0.94	−0.97	+0.36	−0.35
Cd_{2Cu}	−1.08	−2.44	+0.11	−0.82
S_O	−0.76	+0.09	+1.09	−0.39
Se_O	−1.07	−0.49	+1.13	−0.39

level. The actual results given above (cf. Table II) take into account also that the GW quasiparticle energy shifts vary with composition, thereby giving rise to a GW contribution to the composition dependence.

1. Composition dependence of the band-edge energies

In semiconductor alloys, the composition dependence of the band gap and of the band-edge energies is usually described up to quadratic order via a bowing parameter. However, in the composition window $0 \leq x \leq 0.2$ considered in the present work, this dependence is approximately linear. We determine the composition dependence of E_{VBM}, E_{CBM}, and E_g (see Table II) by calculating a single substitution in a 48-atom supercell, both in PBE + U and in GW. The individual contributions are given in Table IV. The potential alignment effects are taken into account to determine the energy lineup between pure and substituted Cu_2O supercells, using all atoms except the substituted ones as references. The change of the crystal volume with composition is taken into account in both the linear extrapolation model and the explicit alloy supercell calculations. Figure 8 shows that both approaches agree
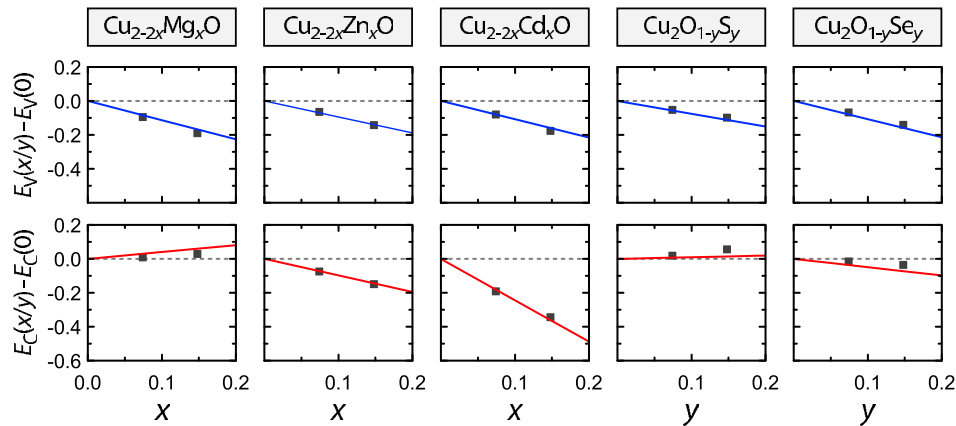

FIG. 8.   Composition dependence of the VBM (top row) and CBM (bottom row) energies. Solid lines represent the extrapolation according to Eq. (2) with PBE + U parameters from Table IV, and the data points are results from explicit alloy supercells.
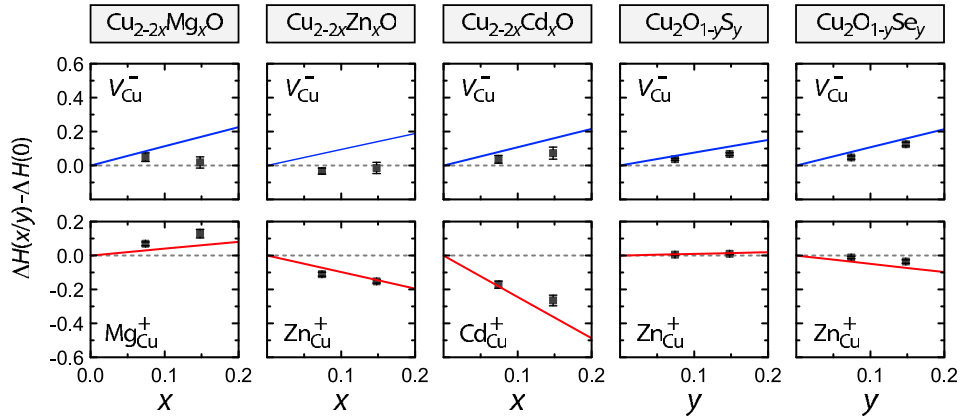
FIG. 9. Composition dependence of the defect formation energy $\Delta H_{D,q}(E_F)$ of the negatively charged V_{Cu} defect (top row) and of the positively charged substitutional cation-site donor (bottom row). The formation energy difference is evaluated for $E_F = E_{VBM}$ in the case of the acceptorlike V_{Cu} defect and for $E_F = E_{CBM}$ in the case of the donorlike cation-site dopant. Solid lines correspond to the extrapolation model using the PBE $+ U$ parameters from Table IV, and data points are from defect calculations in explicit alloy supercells.

very well on the predicted composition dependence of the individual band-edge energies (and, hence, on the predicted band gap). We note that a deviation from the linear proportionality is expected in case of substitutions that cause defect states inside the band gap, which will create a discontinuity of the band-edge energies at x or $y > 0$. This behavior is not observed for the alloy substitutions considered in the present work.

2. Composition dependence of the charged-defect formation energies

In order to extend the dilute-defect model to low and moderate alloy compositions, we consider two effects that affect the defect concentrations. First, the effect of defect-pair association is taken into account by calculating the binding energy and using the law of mass action. Second, the linear extrapolation of the band-edge energies leads to a composition dependence of the charged-defect ($q \neq 0$) formation energy via Eq. (1). We test this model by comparison with defect formation energy calculations in the explicit alloy supercells, averaging over five different defect sites in each of the two alloy representations. Here, we exclude the Cu sites next to the anion (S_O or Se_O) dopants, because the treatment of the pair association already accounts for the lowering of the V_{Cu} formation energy at these sites. Showing the comparison between the extrapolation model and the explicit alloy supercell defect calculations, we see in Fig. 9 that for all cases except V_{Cu} in the cation-substituted case, the model captures well the trends in the composition dependence of ΔH_D and gives reasonable quantitative estimates. In the cation-substituted cases, $\Delta H(V_{Cu})$ calculated in the alloy supercells is lower than the value expected from the extrapolation model. This observation can be explained by the fact that there is a binding energy of, e.g., -0.20 eV between the Zn_{2Cu}

substitution and V_{Cu} at the Cu site nearest to the Zn location. In principle, one can refine the treatment of the pair and complex association to include larger clusters and more configurations with their individual binding energies, e.g., by including a (Zn_{2Cu}-V_{Cu}) complex. However, in practice, one has to cut off the defect interactions at some point, and we feel that the purpose of the present work is better served by including for clarity only the leading mechanisms for defect-pair formation that are shown in Table I. To conclude, the test using explicit alloy supercells confirms that the defect-pair association and the shift of the band-edge energies are the leading effects that need to be included to predict defect formation beyond the dilute limit in low and moderate alloy compositions.

[1] Karl Brunner, Si/Ge nanostructures, Rep. Prog. Phys. **65**, 27 (2002).

[2] Mayeul d'Avezac, Jun-Wei Luo, Thomas Chanier, and Alex Zunger, Genetic-algorithm discovery of a direct-gap and optically allowed superstructure from indirect-gap Si and Ge semiconductors, Phys. Rev. Lett. **108**, 027401 (2012).

[3] Shuji Nakamura, Masayuki Senoh, Naruhito Iwasa, and Shin ichi Nagahama, High-brightness InGaN blue, green and yellow light-emitting diodes with quantum well structures, Jpn. J. Appl. Phys. **34**, L797 (1995).

[4] G. F. Knoll, *Radiation Detection and Measurement*, 3rd ed. (Wiley, New York, 1999).

[5] G. Kinsey, *High-Concentration, III–V Multijunction Solar Cells in Solar Cells and Their Applications* (Wiley, New York, 2010).

[6] J. R. Woodyard, Nonlinear circuit device utilizing germanium, U.S. Patent No. 2,530,110 (14 November 1950).

[7] D. S. Ginley and J. D. Perkins, in *Handbook of Transparent Conductors*, edited by D. S. Ginley, H. Hosono, and D. C. Payne (Springer, New York, 2010).

[8] A. Lindsay and E. P. O'Reilly, Theory of enhanced bandgap non-parabolicity in $GaN_xAs_{1?x}$ and related alloys, Solid State Commun. **112**, 443 (1999).

[9] P. R. C. Kent and Alex Zunger, Theory of electronic structure evolution in GaAsN and GaPN alloys, Phys. Rev. B **64**, 115208 (2001).

[10] Voicu Popescu and Alex Zunger, Effective band structure of random alloys, Phys. Rev. Lett. **104**, 236403 (2010).

[11] John E. Northrup and S. B. Zhang, Dopant and defect energetics: Si in GaAs, Phys. Rev. B **47**, 6791 (1993).

[12] Stephan Lany and Alex Zunger, Dual nature of acceptors in GaN and ZnO: The curious case of the shallow Mg_{Ga} deep state, Appl. Phys. Lett. **96**, 142114 (2010).

[13] J. B. Varley, A. Janotti, and C. G. Van de Walle, Group-V impurities in SnO_2 from first-principles calculations, Phys. Rev. B **81**, 245216 (2010).

[14] A. van de Walle and D. E. Ellis, First-principles thermodynamics of coherent interfaces in samarium-doped ceria nanoscale superlattices, Phys. Rev. Lett. **98**, 266101 (2007).

[15] H. Raebiger, S. Lany, and A. Zunger, Origins of the p-type nature and cation deficiency in Cu_2O and related materials, Phys. Rev. B **76**, 045209 (2007).

[16] D. O. Scanlon, B. J. Morgan, G. W. Watson, and A. Walsh, Acceptor levels in p-type Cu_2O: Rationalizing theory and experiment, Phys. Rev. Lett. **103**, 096405 (2009).

[17] Michael Nolan and Simon D. Elliott, Tuning the transparency of Cu_2O with substitutional cation doping, Chem. Mater. **20**, 5522 (2008).

[18] Sang Woon Lee, Yun Seog Lee, Jaeyeong Heo, Sin Cheng Siah, Danny Chua, Riley E. Brandt, Sang Bok Kim, Jonathan P. Mailoa, Tonio Buonassisi, and Roy G. Gordon, Improved Cu_2O-based solar cells using atomic layer deposition to control the Cu oxidation state at the p-n junction, Adv. Energy Mater. **4**, 1301916 (2014).

[19] Alexander Wagner, Mathieu Stahl, Nikolai Ehrhardt, Andreas Fahl, Johannes Ledig, Andreas Waag, and Andrey Bakin, Oxides for sustainable photovoltaics with earth-abundant materials, Proc. SPIE Int. Soc. Opt. Eng. **8987**, 898726 (2014).

[20] Hiroshi Kawazoe, Masahiro Yasukawa, Hiroyuki Hyodo, Masaaki Kurita, Hiroshi Yanagi, and Hideo Hosono, P-type electrical conduction in transparent thin films of $CuAlO_2$, Nature (London) **389**, 939 (1997).

[21] Geoffroy Hautier, Anna Miglio, Gerbrand Ceder, Gian-Marco Rignanese, and Xavier Gonze, Identification and design principles of low hole effective mass p-type transparent conducting oxides, Nat. Commun. **4**, 2292 (2013).

[22] S. N. Kale, S. B. Ogale, S. R. Shinde, M. Sahasrabuddhe, V. N. Kulkarni, R. L. Greene, and T. Venkatesan, Magnetism in cobalt-doped Cu_2O thin films without and with Al, V, or Zn codopants, Appl. Phys. Lett. **82**, 2100 (2003).

[23] Hannes Raebiger, Stephan Lany, and Alex Zunger, Impurity clustering and ferromagnetic interactions that are not carrier induced in dilute magnetic semiconductors: The case of Cu_2O:Co, Phys. Rev. Lett. **99**, 167203 (2007).

[24] Alberto Mittiga, Enrico Salza, Francesca Sarto, Mario Tucci, and Rajaraman Vasanthi, Heterojunction solar cell with 2% efficiency based on a Cu_2O substrate, Appl. Phys. Lett. **88**, 163502 (2006).

[25] B. K. Meyer, A. Polity, D. Reppin, M. Becker, P. Hering, P. J. Klar, Th. Sander, C. Reindl, J. Benz, M. Eickhoff, C. Heiliger, M. Heinemann, J. Bläsing, A. Krost, S. Shokovets, C. Müller, and C. Ronning, Binary copper oxide semiconductors: From materials towards devices, Phys. Status Solidi (b) **249**, 1487 (2012).

[26] Adriana Paracchino, Vincent Laporte, Kevin Sivula, Michael Grätzel, and Elijah Thimsen, Highly active oxide photocathode for photoelectrochemical water reduction, Nat. Mater. **10**, 456 (2011).

[27] Chris G. Van de Walle and Jörg Neugebauer, First-principles calculations for defects and impurities: Applications to III-nitrides, J. Appl. Phys. **95**, 3851 (2004).

[28] Stephan Lany and Alex Zunger, Dopability, intrinsic conductivity, and nonstoichiometry of transparent conducting oxides, Phys. Rev. Lett. **98**, 045501 (2007).

[29] Stephan Lany and Alex Zunger, Assessment of correction methods for the band-gap problem and for finite-size effects in supercell defect calculations: Case studies for ZnO and GaAs, Phys. Rev. B **78**, 235104 (2008).

[30] Péter Ágoston, Christoph Körber, Andreas Klein, Martti J. Puska, Risto M. Nieminen, and Karsten Albe, Limits for n-type doping in In2O3 and SnO2: A theoretical approach by first-principles calculations using hybrid-functional methodology, J. Appl. Phys. **108**, 053511 (2010).

[31] H. Peng, D. O. Scanlon, V. Stevanović, J. Vidal, G. W. Watson, and S. Lany, Convergence of density and hybrid functional defect calculations for compound semiconductors, Phys. Rev. B **88**, 115201 (2013).

[32] Koushik Biswas and Stephan Lany, Energetics of quaternary III-V alloys described by incorporation and clustering of impurities, Phys. Rev. B **80**, 115206 (2009).

[33] Stephan Lany, Band-structure calculations for the $3d$ transition metal oxides in GW, Phys. Rev. B **87**, 085112 (2013).

[34] J. W. Hodby, T. E. Jenkins, C. Schwab, H. Tamura, and D. Trivich, Cyclotron resonance of electrons and of holes in cuprous oxide, Cu_2O, J. Phys. C **9**, 1429 (1976).

[35] A. F. Wright and J. S. Nelson, Theory of the copper vacancy in cuprous oxide, J. Appl. Phys. **92**, 5849 (2002).

[36] Leah Y. Isseroff and Emily A. Carter, Electronic structure of pure and doped cuprous oxide with copper vacancies: Suppression of trap states, Chem. Mater. **25**, 253 (2013).

[37] J. D. Perkins, A. Mascarenhas, Y. Zhang, J. F. Geisz, D. J. Friedman, J. M. Olson, and S. R. Kurtz, Nitrogen-activated transitions, level repulsion, and band gap reduction in $GaAs_{1-x}N_x$ with $x < 0.03$, Phys. Rev. Lett. **82**, 3312 (1999).

[38] Stephan Lany, Yu-Jun Zhao, Clas Persson, and Alex Zunger, Halogen n-type doping of chalcopyrite semiconductors, Appl. Phys. Lett. **86**, 042109 (2005).

[39] A. Mittiga, F. Biccari, and C. Malerba, Intrinsic defects and metastability effects in Cu_2O, Thin Solid Films **517**, 2469 (2009).

[40] U. V. Desnica, Doping limits in II-VI compounds—challenges, problems and solutions, Prog. Cryst. Growth Charact. Mater. **36**, 291 (1998).

[41] A. Zakutayev, T. R. Paudel, P. F. Ndione, J. D. Perkins, S. Lany, A. Zunger, and D. S. Ginley, Cation off-stoichiometry leads to high p-type conductivity and enhanced transparency

in Co_2ZnO4 and Co2NiO4 thin films, Phys. Rev. B **85**, 085204 (2012).

[42] G. B. González, T. O. Mason, J. S. Okasinski, T. Buslaps, and V. Honkimäki, Determination of the solubility of tin in indium oxide using in situ and ex situ x-ray diffraction, J. Am. Ceram. Soc. **95**, 809 (2012).

[43] R. Singh, D. Doppalapudi, T. D. Moustakas, and L. T. Romano, Phase separation in InGaN thick films and formation of InGaN/GaN double heterostructures in the entire alloy composition, Appl. Phys. Lett. **70**, 1089 (1997).

[44] Archana Subramaniyan, John D. Perkins, Ryan P. O'Hayre, Stephan Lany, Vladan Stevanović, David S. Ginley, and Andriy Zakutayev, Non-equilibrium deposition of phase pure Cu_2O thin films at reduced growth temperature, APL Mater. **2**, 022105 (2014).

[45] Stephan Lany and Alex Zunger, Accurate prediction of defect properties in density functional supercell calculations, Model. Simul. Mater. Sci. Eng. **17**, 084002 (2009).

[46] Andriy Zakutayev, Nicola H. Perry, Thomas O. Mason, David S. Ginley, and Stephan Lany, Non-equilibrium origin of high electrical conductivity in gallium zinc oxide thin films, Appl. Phys. Lett. **103**, 232106 (2013).

[47] Andriy Zakutayev, Frank J. Luciano, Vincent P. Bollinger, Ajaya K. Sigdel, Paul F. Ndione, John D. Perkins, Joseph J. Berry, Philip A. Parilla, and David S. Ginley, Development and application of an instrument for spatially resolved seebeck coefficient measurements, Rev. Sci. Instrum. **84**, 053905 (2013).

[48] A. Zakutayev, J. D. Perkins, P. A. Parilla, N. E. Widjonarko, A. K. Sigdel, J. J. Berry, and D. S. Ginley, Zn-Ni-Co-O wide-band-gap p-type conductive oxides with high work functions, MRS Commun. **1**, 23 (2011).

[49] G. Mandel, Self-compensation limited conductivity in binary semiconductors. i. theory, Phys. Rev. **134**, A1073 (1964).

[50] Claudia Malerba, Francesco Biccari, Cristy Leonor Azanza Ricardo, Mirco D'Incau, Paolo Scardi, and Alberto Mittiga, Absorption coefficient of bulk and thin film Cu_2O, Sol. Energy Mater. Sol. Cells **95**, 2848 (2011).

[51] L. Papadimitriou, DLTS evaluation of nonexponential transients of defect levels in cuprous oxide (Cu_2O), Solid State Electron. **36**, 431 (1993).

[52] P. E. Blöchl, Projector augmented-wave method, Phys. Rev. B **50**, 17953 (1994).

[53] G. Kresse and D. Joubert, From ultrasoft pseudopotentials to the projector augmented-wave method, Phys. Rev. B **59**, 1758 (1999).

[54] John P. Perdew, Kieron Burke, and Matthias Ernzerhof, Generalized gradient approximation made simple, Phys. Rev. Lett. **77**, 3865 (1996).

[55] S. L. Dudarev, G. A. Botton, S. Y. Savrasov, C. J. Humphreys, and A. P. Sutton, Electron-energy-loss spectra and the structural stability of nickel oxide: An LSDA + U study, Phys. Rev. B **57**, 1505 (1998).

[56] Vladan Stevanović, Stephan Lany, Xiuwen Zhang, and Alex Zunger, Correcting density functional theory for accurate predictions of compound enthalpies of formation: Fitted elemental-phase reference energies, Phys. Rev. B **85**, 115104 (2012).

[57] M. Shishkin and G. Kresse, Implementation and performance of the frequency-dependent GW method within the PAW framework, Phys. Rev. B **74**, 035101 (2006).

[58] Georgy Samsonidze, Manish Jain, Jack Deslippe, Marvin L. Cohen, and Steven G. Louie, Simple approximate physical orbitals for GW quasiparticle calculations, Phys. Rev. Lett. **107**, 186404 (2011).

[59] C. Friedrich, M. C. Müller, and S. Blügel, Band convergence and linearization error correction of all-electron GW calculations: The extreme case of zinc oxide, Phys. Rev. B **83**, 081101 (2011).

[60] Ji ř í Klimeš, Merzuk Kaltak, and Georg Kresse, Predictive GW calculations using plane waves and pseudopotentials, Phys. Rev. B **90**, 075125 (2014).

[61] Vladan Stevanović, Stephan Lany, David S. Ginley, Willam Tumas, and Alex Zunger, Assessing capability of semiconductors to split water using ionization potentials and electron affinities only, Phys. Chem. Chem. Phys. **16**, 3706 (2014).

[62] Kazunori Iwamitsu, Shingo Aihara, Tomoshige Shimamoto, Atsuhiro Fujii, and Ichiro Akai, Wavelength-modulated excitonic spectra in green series of Cu_2O thin films sandwiched by MgO plates, Phys. Status Solidi (c) **9**, 2489 (2012).